

Analysis and calibration techniques for superconducting resonators

Giuseppe Cataldo, Edward J. Wollack, Emily M. Barrentine, Ari D. Brown, S. Harvey Moseley, and Kongpop U-Yen

Citation: *Review of Scientific Instruments* **86**, 013103 (2015); doi: 10.1063/1.4904972

View online: <http://dx.doi.org/10.1063/1.4904972>

View Table of Contents: <http://scitation.aip.org/content/aip/journal/rsi/86/1?ver=pdfcov>

Published by the [AIP Publishing](#)

Articles you may be interested in

[Nanoscale constrictions in superconducting coplanar waveguide resonators](#)

Appl. Phys. Lett. **105**, 162601 (2014); 10.1063/1.4899141

[In situ broadband cryogenic calibration for two-port superconducting microwave resonators](#)

Rev. Sci. Instrum. **84**, 034706 (2013); 10.1063/1.4797461

[Nonlinear effects in YBa₂Cu₃O_{7-x} microstrip resonators on sapphire](#)

Appl. Phys. Lett. **79**, 4174 (2001); 10.1063/1.1425460

[Microwave intermodulation of a superconducting disk resonator](#)

J. Appl. Phys. **86**, 4055 (1999); 10.1063/1.371330

[Analysis of superconducting microstrip resonator at various microwave power levels](#)

J. Appl. Phys. **81**, 6272 (1997); 10.1063/1.364415



Analysis and calibration techniques for superconducting resonators

Giuseppe Cataldo,^{a)} Edward J. Wollack, Emily M. Barrentine, Ari D. Brown,
S. Harvey Moseley, and Kongpop U-Yen
NASA Goddard Space Flight Center, Greenbelt, Maryland 20771, USA

(Received 14 November 2014; accepted 11 December 2014; published online 8 January 2015)

A method is proposed and experimentally explored for *in-situ* calibration of complex transmission data for superconducting microwave resonators. This cryogenic calibration method accounts for the instrumental transmission response between the vector network analyzer reference plane and the device calibration plane. Once calibrated, the observed resonator response is analyzed in detail by two approaches. The first, a phenomenological model based on physically realizable rational functions, enables the extraction of multiple resonance frequencies and widths for coupled resonators without explicit specification of the circuit network. In the second, an ABCD-matrix representation for the distributed transmission line circuit is used to model the observed response from the characteristic impedance and propagation constant. When used in conjunction with electromagnetic simulations, the kinetic inductance fraction can be determined with this method with an accuracy of 2%. Datasets for superconducting microstrip and coplanar-waveguide resonator devices were investigated and a recovery within 1% of the observed complex transmission amplitude was achieved with both analysis approaches. The experimental configuration used in microwave characterization of the devices and self-consistent constraints for the electromagnetic constitutive relations for parameter extraction are also presented. © 2015 AIP Publishing LLC. [<http://dx.doi.org/10.1063/1.4904972>]

I. INTRODUCTION

Recent advances in astrophysical instrumentation have introduced superconducting microwave resonators for read-out and the detection of infrared light.¹⁻⁴ An essential element of the successful development of cameras employing these resonant structures is to accurately and efficiently characterize their properties. More broadly, precision measurements of quality factors Q of superconducting resonators are desired in the context of microwave kinetic inductance detectors (MKIDs) device physics,⁵ quantum computing,⁶ and the determination of low-temperature materials properties.^{7,8} At sub-kelvin temperatures, the quality factors are generally determined by measuring and fitting the transmission data over the relatively narrow bandwidth defined by the response of a single resonator.⁹ In this setting, the fidelity of the observed response can be limited by the intervening instrumentation between the device under test (DUT) and the measurement reference plane.

In physically modeling the electrical response of these circuits, a lumped-element approximation can be applied when the electrical size of the elements and their interconnections is small compared to a wavelength. This consideration ensures that the structures are not self-resonant. More generally, a transmission line approximation enables one to treat distributed elements with one dimension greater than a fraction of a wavelength in scale. However, when the electromagnetic fields and phases within the circuit elements are uniform and uncoupled, the lumped and distributed approaches are identical.¹⁰ It is not uncommon for “lumped elements” to have a significant internal phase delay in practical microwave

devices. For “capacitive” elements synthesized from electrically small transmission line lengths, this effect can be small, but “inductive” elements inherently possess a finite internal phase delay by design. The utility of this iconic lumped picture primarily resides in its conceptual simplicity as opposed to the end accuracy and fidelity of the physical representation.

This being said, analytical methods based on lumped-element approximations are commonly used to analyze scattering parameters of resonators and compute their Q factors.¹¹⁻¹⁶ These expressions are derived from LCR circuit representations and are based on the assertion of weak coupling between resonators to simplify the analysis. These formulations employ simplified functional forms for the transmission, S_{21} , and are suited for approximating the response near resonance for high-quality-factor lumped circuits.

A detailed review of fitting methods is offered in Ref. 9, where several methods are presented for fitting the S_{21} magnitude to different models, neglecting the measured phase. These methods do not deal with the alterations that the data incur in the real measurement scenario, such as crosstalk between cables and/or coupling structures, the resonator coupling ports not being coincident with the reference plane of the measurements, and the presence of and coupling to nearby resonators. Many of the methods described, which attempt to correct for these effects on S_{21} , remain sensitive to the details of fitting in the complex plane.^{9,17,18} In this work, we strive to address these issues by using a transmission line representation to simultaneously analyze multiple coupled resonators and present a calibration methodology to remove non-ideal instrument artifacts.

The resonator’s transmission amplitude and phase can be characterized with a vector network analyzer (VNA). Ideally, the VNA calibration reference plane or “test port” would be

^{a)}Electronic mail: Giuseppe.Cataldo@NASA.gov

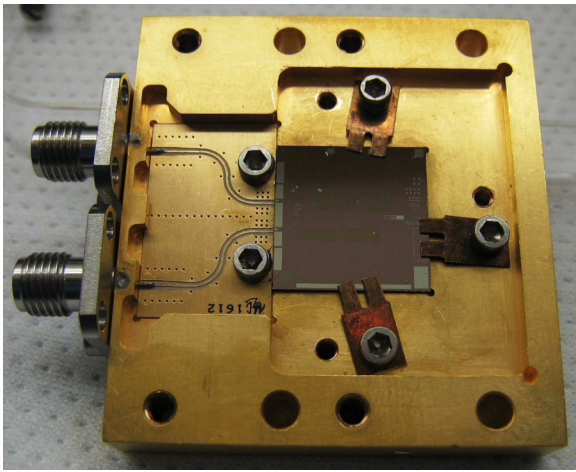


FIG. 2. Resonator chip, printed circuit CPW transition board, and SMA connector interface mounted in the test package. The package cover has been removed for clarity.

blocking filters²³ for realization of the terminations for the DUT. This configuration would also be desirable or necessary for the characterization of devices with low saturation power. The output signal was routed via copper and superconducting niobium-titanium (NbTi) coaxial cables through a CTD1229K PamTech circulator, which was mounted on the 2-K stage of the cryostat. This circulator operates with a return loss ≥ 20 dB between 2.5 and 4 GHz. From the isolator, the output signal was routed to an AF S3-02000400-08-CR-4 MITEQ amplifier mounted on the 2-K stage.

III. MEASUREMENT METROLOGY MOTIVATION

We define the response at the “VNA reference plane” as observed through a microwave path to the “device calibration plane” as the instrument baseline (Fig. 1). In a perfectly impedance-matched and lossless instrument, the magnitude of the complex transmission amplitude, S_{21} , for a thru connection would be unity. In practice, the instrument baseline has frequency structure and amplitude set by the details and quality of the intervening transmission line components. These instrumental artifacts need to be addressed in calibration to provide an unbiased measurement of the device response.

A Short-Open-Line-Thru (SOLT) calibration was used to calibrate the PNA-X in 3.5-mm coax at the VNA reference plane defined in Fig. 1. After recording the complex transmission measurements, an *in-situ* calibration process was used in order to move the reference plane to the device calibration plane. In the calibration process adopted here, we assume that the test device sees a matched termination. For the 2-resonator data, this condition is realized by a 7-dB attenuator and isolator. For the baseline removal approach described here to be successful, the response of the attenuators, transmission line media, and amplifiers used in the system should be smooth functions over the spectral band of interest relative to the test-device frequency response.

It is notable that in this implementation, the feed transmission line structure in the device under test plays a dual role: It allows excitation and read-out of the sharply peaked

circuit response of interest, and off resonance serves as a controlled impedance reference (thru line) standard to specify the system’s gain as a function of frequency. The underlying approach explored in this work for baseline removal has its roots in a variety of analogous instruments such as frequency-swept reflectometry²⁴ and spectral baseline correction in radio astronomy.^{25,26} In particular, the differential reflectometer configuration used for cavity characterization²⁷ provides insight in this context. In this method, the baseline is explicitly removed on resonance by comparing the response of a waveguide cavity with that of a short-circuit via the difference port of a magic-T power divider. Adjustment of the short position in this bridge reflectometer circuit reveals the interaction between the resonator and the baseline shape. More importantly, this points to the role of the resonator phase and baseline shape on the observed scattering parameters at resonance.

IV. VNA TRANSMISSION DATA CALIBRATION

For a single resonator or multiple well-separated resonators, the response can be well reproduced by a Lorentzian line shape. In the presence of multiple resonances, their mutual interaction as well as the interaction with the continuum can result in a Fano spectral response.^{28–32} This effect can also be experimentally observed as an interaction between the resonators with the relatively broad Fabry-Perot resonances resulting from standing waves in the system. Such reflections produce the dominant spectral variation in the observed instrument baseline and can be mitigated by minimizing the transmission line lengths and suitably terminating the reflections with matched attenuators and circulators at the instrument termination plane. In calibrating the spectra, an unbiased removal of these artifacts is desired.

As an example of the calibration process, we use the data from the CPW feedline coupled to the two Mo₂N resonators. Figure 3(a) shows the real and imaginary components of the transmission, S_{21} , at the VNA reference plane as a function of frequency. It can be seen that the characteristic scale of the baseline variations is much larger than the resonator response in frequency. To calibrate the VNA data *in-situ*, the following steps are performed:

1. fit of the complex baseline (Fig. 3(c));
2. normalization of the transmission’s real and imaginary parts (Figs. 3(c) and 3(d));
3. correction for variations in gain and relocation of the reference plane at the DUT by ratioing out the complex baseline fit (Figs. 3(e) and 3(f)).

In general, the baseline can have an unpredictable shape as determined by the details of the reflections occurring throughout the instrument and its components. The complex baseline, $S_{21,bas}$, was modeled analytically and a Fourier series was found to be a convenient and physically motivated representation of its response:

$$S_{21,bas} = \sum_{j=1}^n A_j \cdot \exp(id_j\omega). \quad (1)$$

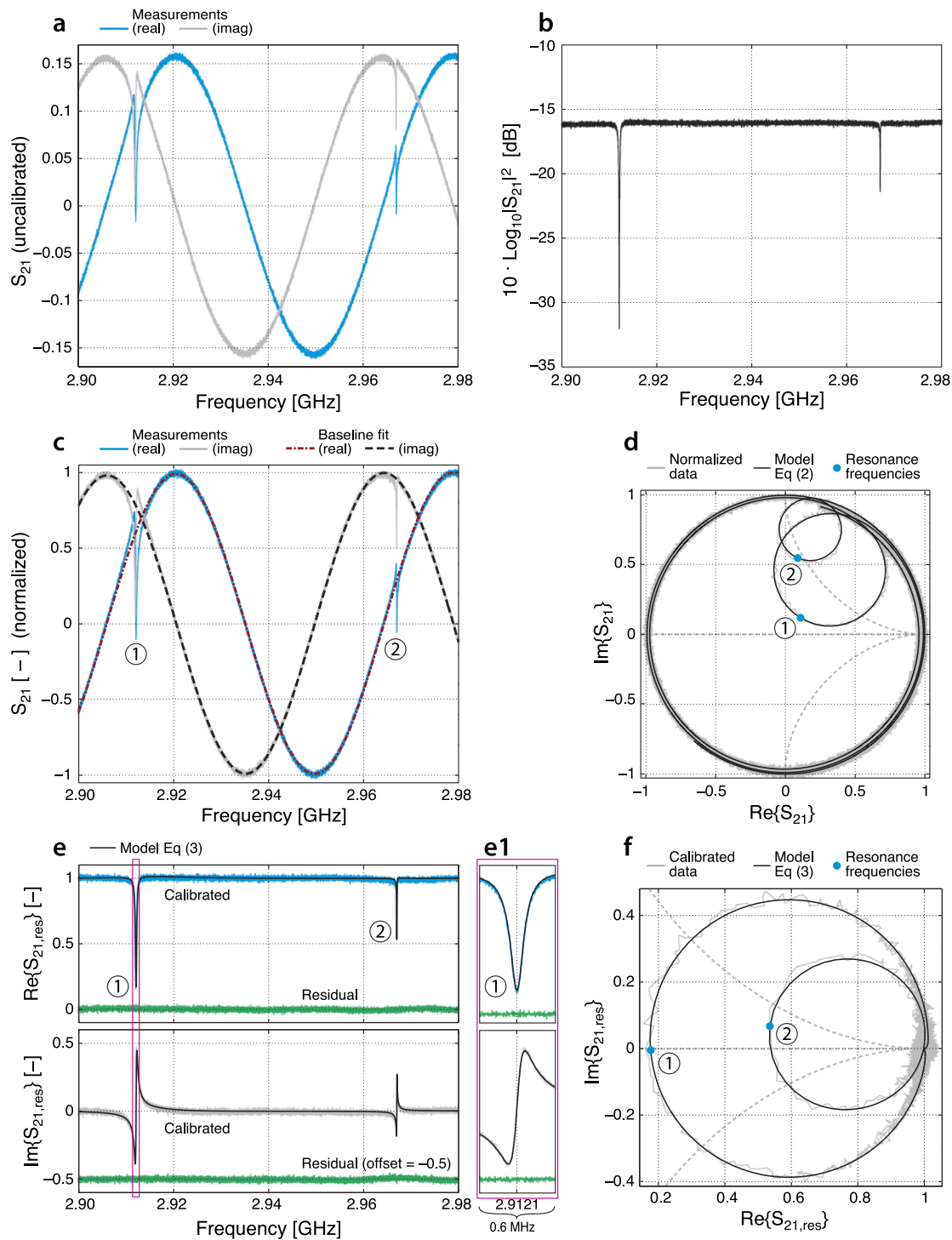


FIG. 3. Measurement calibration overview. (a) Complex S_{21} data for the DUT as observed at the VNA reference plane. (b) From the perspective of the DUT, the magnitude of the response is uncalibrated due to the amplifiers, attenuators, and other microwave elements in the system. (c) The measured transmission spectrum is normalized by forcing its amplitude to be equal to unity far from the resonator responses. The baseline fit is displayed for ease of comparison. (d) The normalized transmission data are shown on a Smith chart. The baseline variation with frequency can be seen as a deviation in the S_{21} from unity far from the resonator response. (e) After removing the complex baseline and specifying the device-calibration-plane phase, the calibrated data are used to fit an analytical model, and the residuals are shown. (f) The Smith chart shows the two resonance loops going through (1,0) after calibration.

In Eq. (1), A_j is a complex coefficient, d_j a time delay, and ω the angular frequency. In the case presented, $n = 4$ terms were found to be sufficient to adequately sample the baseline and appropriately constrain its properties. A fit to the 30 000 measured data points resulted in a reduced $\chi^2 = 0.9973$. Differences in experimental configuration or changes in the

desired calibration spectral range may lead to alternative forms for Eq. (1).

The second step in data calibration consists of uniquely specifying the complex gain amplitude between the VNA reference plane and the device calibration plane so that the S_{21} real and imaginary components in Fig. 3(a) lie between ± 1 .

This normalization factor was found to be approximately 6.32 by forcing the transmission amplitude to be equal to unity far from the resonator response. The normalized measurements and modeled data are presented in the Smith chart in Fig. 3(d).

Finally, the complex baseline, $S_{21,bas}$, was removed from the data through Eq. (1) to eliminate the influence of reflections and move the reference plane to the DUT. By looking at the topology of the instrument, the error matrices introduced by the connections between the reference plane and the device under test in the cryostat are in series. From the properties of signal flow graphs,^{24,33} the uncalibrated transmission coefficient, S_{21} , at the VNA reference plane is therefore the product of the following scattering matrix elements:

$$S_{21} = S_{21,bas} \cdot S_{21,res}, \quad (2)$$

where $S_{21,res}$ refers to the desired calibrated response of the resonator device under test.

V. PHENOMENOLOGICAL RESONATOR MODEL

With the baseline correction applied, the calibrated data (Figure 3(e)) were modeled in order to extract the characteristic resonant frequencies and line widths. The feedline and resonator model for the packaged device can be represented as a realizable causal filter as follows:

$$S_{21,res} = 1 + \sum_{j=1}^M \frac{a_{0,j} + a_{1,j}x_j + a_{2,j}x_j^2 + \dots}{1 + ix_j + b_{2,j}x_j^2 + \dots}, \quad (3)$$

where, for each $j = 1, \dots, M$ (M being the total number of resonators), $x_j = Q_{tot,j} \cdot (\omega/\omega_{o,j} - \omega_{o,j}/\omega)$ and $Q_{tot,j}$ is the total loaded quality factor defined as $Q_{tot,j} = \omega_{o,j}/\Gamma_j$. For each resonator, therefore, the fitting parameters are: the $a_{k,j}$ and $b_{k,j}$ complex coefficients ($k = 0, 1, 2, \dots, j = 1, \dots, M$), the resonance frequency $\omega_{o,j}$, and the full width at half power Γ_j . Here, we use $k = 2$ in specifying the order of the polynomial.

The functional form of Eq. (3) exhibits several features. First, its second-order terms in both the numerators and denominators allow for reproduction of the resonator responses, thereby enabling the representation of a physically realizable, distributed circuit network.³⁴ Second, its causality is assured by the degree of the numerator not being greater than that of the denominator, which allows the functional form to satisfy the Kramers-Kronig relations.³⁵ Far removed from the resonators, $S_{21,res} \rightarrow 1 + i0$ and the transmission represents an ideal thru line. It was verified that our second-order model approached this limit without additional terms to avoid increasing the number of parameters and the computational effort. Finally, this functional form enables one to simultaneously fit any number of resonators while formally taking into account their physical interactions.

TABLE I. Parameter summary for the 2-resonator analytical model.^a

j (-)	$a_{0,j}$ (-)	$a_{1,j}$ (-)	$a_{2,j}$ (-)	$b_{2,j}$ (-)	$\omega_{o,j}/(2\pi)$ (GHz)	$\Gamma_j/(2\pi)$ (kHz)
1	$-0.7345 + i 0.1029$	$-0.0440 + i 0.0879$	$-0.0008 - i 0.0009$	$-0.0120 - i 0.0048$	$2.9121 \dots \pm 7 \times 10^{-9}$	139.02 ± 0.01
2	$-0.5496 - i 0.0463$	$-0.4737 + i 2.1868$	$-2.1104 - i 2.4638$	$30.0366 - i 13.2458$	$2.9670 \dots \pm 60 \times 10^{-9}$	50 ± 2

^aIn the analysis double precision (16 digits) was used; however, for clarity here we only show the leading digits.

Rewriting x_j in the equivalent form, $x_j = Q_{tot} \cdot (\omega_{o,j}/\omega) \cdot (\omega/\omega_{o,j} + 1) \cdot (\omega/\omega_{o,j} - 1)$, reveals a commonly employed approximation, $x_j \approx 2Q_{tot} \cdot (\omega/\omega_{o,j} - 1)$, near resonance. This form can be viewed as an asymptotic expansion in powers of $1/Q_{tot}$ which modifies the position of the resonant frequency in the complex plane.³⁶ When Eq. (3) is evaluated in this limit, the expressions reduce to the first-order lumped-circuit treatments described in the literature for a single resonator in transmission.^{11,12,37} However, we find that to faithfully reproduce the interactions between resonators over a wide spectral bandwidth, the full functional form presented here is required.

A. Analysis of the 2-resonator dataset

Equation (3) was used to fit the calibrated data by means of a least-squares curve fitting routine based on a trust-region reflective Newton method.^{38,39} Constraints were given in the form of global lower and upper bounds for each $\Gamma > 0$ and ω_o . The starting guess for each Γ was chosen close to the actual value, which can be readily determined by estimating each resonator's spectral width. The initial guess for the resonance frequency, on the other hand, corresponds to the frequency values where the observed S_{21} has minima. The results are shown in Fig. 3(e) (black line) for both components. The residuals on the real and imaginary parts are comparable to the normally distributed noise level in the measured data with a reduced $\chi^2 = 0.9987$ and a standard deviation of $\sigma = 0.0155$. A Smith chart is provided in Fig. 3(f), which shows that the two circles touch each other at (1,0) with a relative rotation of about 7° caused by the phase delay in the feedline length between the two resonators. Because of the noise in the measured data and the residual systematic errors in the baseline fit, the data around (1,0) converge to this point within a radius of 0.04. The estimated values for the fitting parameters of each resonator are summarized in Table I.

The internal and coupling Q factors were calculated using the following equations:^{40,41}

$$Q_{i,j} = \frac{Q_{tot,j}}{1 - D_j}, \quad (4)$$

$$Q_{c,j} = \frac{Q_{tot,j}}{D_j}, \quad (5)$$

where D_j represents the diameter of the circle associated with each resonator (Fig. 3(f)). The Q -factor values are shown in Table II.

B. Analysis of the 14-resonator dataset

A 14-resonator CPW dataset was also studied (see Figs. 4(a) and 4(b)). In this example, the resonators span a spectral range of about 45 MHz with two pairs of resonators

TABLE II. Q factors for the 2-resonator analytical model.

j (-)	$Q_{tot,j}$ (-)	$Q_{i,j}$ (-)	$Q_{c,j}$ (-)
1	$20,948 \pm 1$	$107,583 \pm 2$	$26,013 \pm 1$
2	$59,400 \pm 180$	$109,500 \pm 330$	$129,800 \pm 390$

strongly interacting with each other, namely, resonators 5 and 6 and 9 and 10. The analysis of this dataset was challenging because, for high values of Q_{tot} , the denominator of Eq. (3) approaches an indeterminate form of the type $[0 \cdot \infty]$, which can result in numerical instability. In addition, the parameters of interest span 6 orders of magnitude leading to an ill-conditioned Hessian matrix for the system.

Equation (3) was used to fit the calibrated data by means of a least-squares curve fitting routine based on a trust-region reflective Newton method with a diagonal preconditioning of the conjugate gradient. To help the algorithm with convergence, all Γ_j and $\omega_{o,j}$ ($j = 1, \dots, 14$) were provided with lower and upper bounds, namely, $0 < \Gamma_j \leq \Gamma_{max}$ and $\omega_{min} \leq \omega_{o,j} \leq \omega_{o,max}$ for $j = 1, \dots, 14$. Here, $\Gamma_{max} = 10$ MHz, well above the largest Γ_1 (≈ 1.6 MHz). The minimum angular frequency is

$\omega_{min} = 2.5040$ GHz and the maximum resonance frequency, $\omega_{o,max}$, was set not to exceed a distance of $10 \times \Gamma_{14}$ from the last resonance frequency. For the highest- Q resonators (i.e., the highest frequencies in the recorded transmission spectra), the model is more sensitive to changes in $\omega_{o,j}$. This choice for the bounds helped the algorithm in identifying solutions within the desired range of parameters and converged after < 300 iterations.

The model represented by Eq. (3) recovers the calibrated data within an accuracy of $< 1\%$ (Figs. 4(c) and 4(d)) with a reduced $\chi^2 = 0.9985$ and a standard deviation $\sigma = 0.0027$, thus proving to be a robust method to analyze numerous, strongly coupled resonators. In this dataset, the range of quality factors spans more than two orders of magnitude, e.g., $2,300 < Q_c < 630,000$. A particular challenge noted in this existing dataset was that the observed spectral range was suboptimal. From an experimental design perspective, the phase variation of the DUT and the baseline need to be appropriately sampled and possess differing spectral signatures to enable independent reconstruction from the measured dataset. By using the modeled response as noiseless input to the fitting algorithm, it was found that the spectral range of this dataset should have been extended by 30% to minimize the calibration

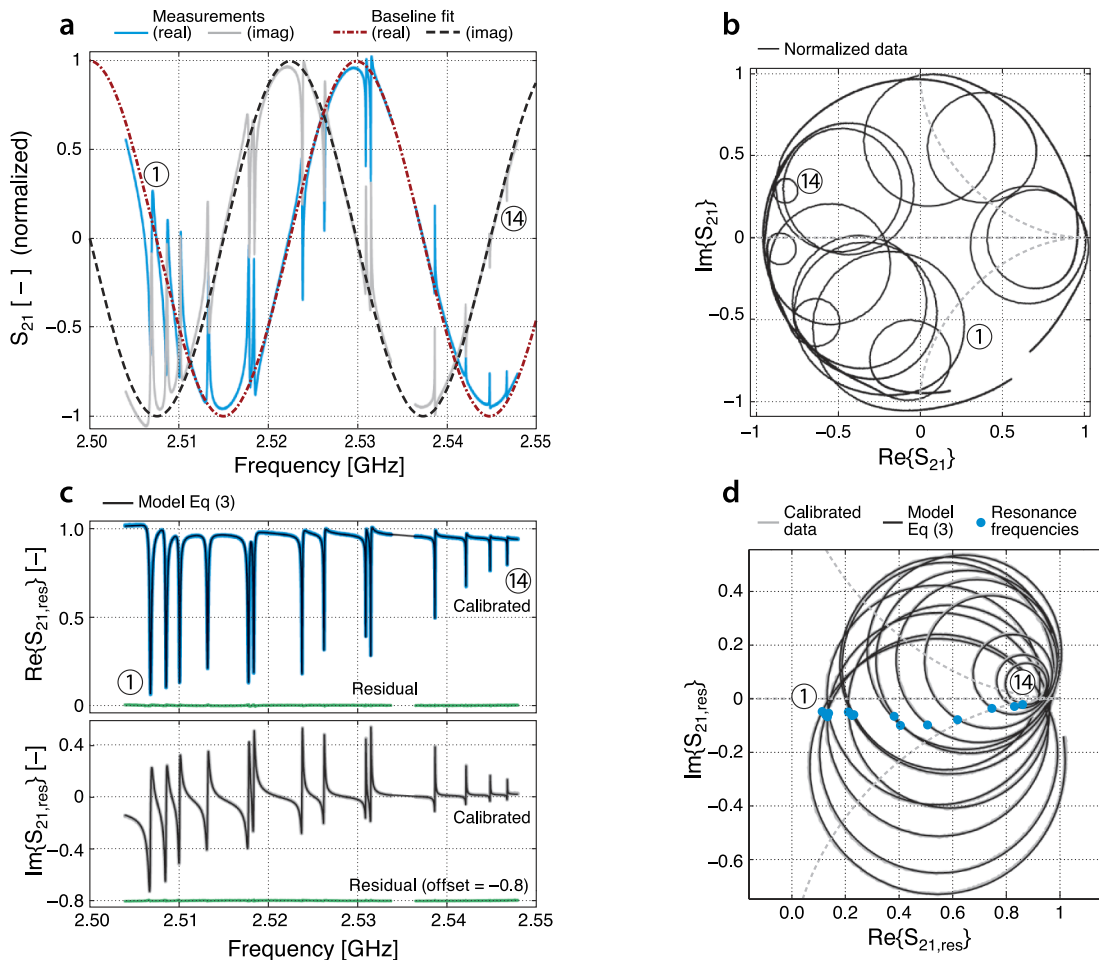


FIG. 4. Results for the 14-resonator CPW dataset. (a) Normalized transmission data and baseline fit. (b) Smith chart representation of the normalized transmission data. (c) Calibrated transmission data and analytical model. The achieved residuals are smaller than 1%. (d) Smith chart showing the calibrated 14-resonator data wrapping around (1,0). Note: The 14-resonator CPW dataset was acquired in two discrete sections and a small gap in the measured transmission spectra is present at ≈ 2.535 GHz.

error with this algorithm. This increase in spectral range would enable the responses of the resonator wings and the baseline to be sufficiently decoupled to achieve an unbiased amplitude calibration.

VI. ABCD-MATRIX MODEL

The phenomenological resonator model, based on Eq. (3) and discussed in Sec. V, is useful and sufficient if one needs to know the center frequencies and the resonators' Q factors. Clearly, there are many quasi-TEM structures such as microstrip, CPW, or other transmission line types which can lead to the observed response. Since the phenomenological resonator model is blind to the details of the realization, a distributed transmission line representation needs to be employed in order to probe the internal structure of the circuit. Here, the impedance, propagation constant, and lengths are used to characterize the circuit response in an ABCD or chain-matrix formulation. In this process, specifically, the impedance and propagation constant are used as parameters to fit the transmission data.

Although coupling to higher-order modes (e.g., losses to radiation, surface waves, and parasitic coupling between elements) can influence the underlying network topology, in the formulation used here, we assume single-mode propagation and rely upon the specification of the circuit network. This process is related to "de-embedding" or the process of inferring the response of a device under test when electrical properties of the intervening structure (in this case, the feedline coupling structure) are known.⁴² Elegant implementations of such concepts in the context of scalar millimeter-wave circuit metrology are described in Refs. 43 and 44.

To model the 2-resonator device response below the instrument termination plane (Fig. 1), 29 transmission line elements were used. For each line section, the physical lengths, l , were known to a micron accuracy from the photolithographic mask, while the characteristic impedances, Z_o , and the propagation constant, γ , were simulated with HFSS (High Frequency Structure Simulator). For simplicity, the two coupling capacitors were modeled as lumped elements and their capacitances also simulated with HFSS ($C_{c1} \approx 53$ fF and $C_{c2} \approx 23$ fF). The detailed description of the ABCD-matrix model can be found in the Appendix.

Substituting the numerical values of each transmission line element into Eq. (A4) and cascading through Eq. (A3) yields the ABCD parameters of the entire transmission line circuit. These parameters were used in Eq. (A2) to evaluate the modeled transmission response, S_{21} . A challenge of this method lies in the difficulty of fully specifying the elements of the system at cryogenic temperatures. To simplify the extent of the system to be characterized, the instrument calibration plane was chosen to approximate a matched termination as close as feasible to the packaged device under test.

In addition, as a cross-check of the baseline correction obtained by fitting, the elements leading to this instrumental response were computed with the ABCD-matrix model and agreed to within a 5% accuracy with the measured transmission

line coaxial-cable lengths given nominal literature values for the Teflon dielectric. Experimental investigation revealed that the superconducting NbTi thermal break cable was the limiting element in the uncorrected baseline response. In fitting, it was found that the characteristic impedance of this line was $\approx 60 \Omega$. This section of cable was subsequently inspected and a gap in the Teflon dielectric was noted to be consistent with these observations.

A. Transmission line parameter extraction

For the transmission line structures, the characteristic impedance, Z_o , and propagation constant, γ , are functions of the effective permittivity, $\epsilon_{r,\text{eff}}$, and permeability, $\mu_{r,\text{eff}}$, in the medium. In particular, Z_o is a function of the transmission line geometry proportional to the relative wave impedance in the medium, $Z_n \equiv (\mu_{r,\text{eff}}/\epsilon_{r,\text{eff}})^{1/2}$, and γ is defined such that

$$\gamma^2 \equiv -\left(\frac{\omega}{c}\right)^2 \cdot (\epsilon_{r,\text{eff}} \cdot \mu_{r,\text{eff}}) = -\left(\frac{\omega}{c}\right)^2 \cdot n_{\text{eff}}^2, \quad (6)$$

where ω is the angular frequency, c the speed of light in vacuum, and n_{eff} is the effective index in the medium. For microstrip, the effective permittivity and permeability are explicitly defined as

$$\epsilon_{r,\text{eff}} \equiv \frac{C(\epsilon_1, \epsilon_2)}{C(\epsilon_o, \epsilon_o)}, \quad \mu_{r,\text{eff}} \equiv \frac{L(\mu_1, \mu_2)}{L(\mu_o, \mu_o)}, \quad (7)$$

where the capacitance, C , and the inductance, L , per unit length are measures of the electromagnetic energy stored in the transmission line.^{45,46} To find the effective constitutive relations, these functions are evaluated in the presence and absence of the dielectric and superconducting media, respectively. Here, ϵ_2 refers to the monocrystalline silicon substrate, ϵ_1 to the superstrate dielectric, μ_1 to the centerline, μ_2 to the ground plane metallization, and ϵ_o and μ_o are the permittivity and permeability of free space (see Fig. 5). For other transmission line structures, analogous formulations of Eq. (7) can be defined for the constitutive parameters.

This parameterization results in $\epsilon_{r,\text{eff}}$ and $\mu_{r,\text{eff}}$ becoming implicit functions of the line's materials properties and cross-sectional geometry. The imaginary component of $\mu_{r,\text{eff}}$ was taken as zero. An effective dielectric loss tangent $\approx 1.8 \times 10^{-5}$ was observed in fitting the observed microstrip resonator spectra. This is consistent with the bound on the dielectric loss tangent, $< 5 \times 10^{-5}$, at 2.2 K for a similar (1.45- μm -thick) silicon sample used as a Nb microstrip ring resonator at 4.7 GHz. As discussed in Ref. 48, upon cooling to cryogenic temperatures, the bulk resistivity silicon ($\rho \geq 1 \text{ k}\Omega\text{-cm}$ for these samples) freezes out and the intrinsic loss mechanisms in silicon dominate at microwave frequencies. The achievable thicknesses and high uniformity ($\pm 0.013 \mu\text{m}$) of the monocrystalline silicon wafers⁴⁷ employed in this investigation enable its use as an ultra-low-loss controlled-impedance microwave substrate. The observed loss in the circuit can have contributions from the bulk properties of the silicon layers, the bisbenzocyclobutene (BCB) wafer bonding agent, two-level systems in the silicon oxide layer, and conversion to surface and radiation modes. In addition, residual coupling to the electromagnetic environment could contribute to the observed loss, in particular for higher Q factors. Although a detailed

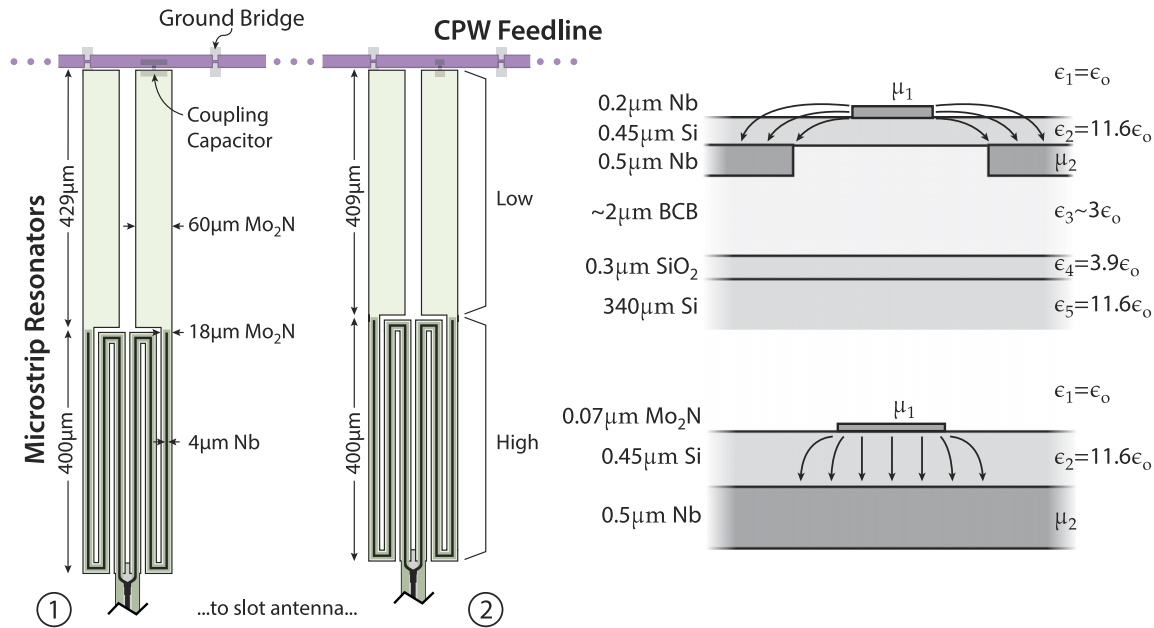


FIG. 5. Left: Layout for the 2-resonator chip. The stepped-impedance resonators are coupled to a CPW feedline and are realized from low- and high-impedance microstrip transmission lines. The “ground bridge” prevents excitation of the asymmetric slotline mode on the CPW feedline structure. The 4- μm Nb microstrip line uses SiO_2 as a dielectric insulator (0.1- μm thick) from the Mo_2N layer. This transmission line structure is not explicitly used at microwave frequencies but enables millimeter wave coupling to a dual-slot antenna.²² Right: A simplified cross-sectional view of the coplanar waveguide (top) and microstrip transmission line (bottom) geometries used in modeling the electromagnetic response. The permittivity for the dielectric layers and the permeability for the lines are indicated. The arrows indicate the electric field and its dominant modal symmetry. The microwave dielectric substrate (0.450 \pm 0.025- μm thick, 100-mm diameter) is monocrystalline silicon.⁴⁷

breakdown of the contributions to the observed loss is possible by investigating the performance as a function of geometry and temperature, this was not attempted here. Thus, in ascribing the entire observed loss to the dielectric, the above-mentioned loss tangent represents a conservative upper bound to that of monocrystalline silicon.

In fitting, for each transmission line type (high or low), a global characteristic impedance and phase velocity were employed. The low-impedance lines have a width of 60 μm , whereas the high-impedance lines have a width of 18 μm . Electromagnetic simulations were performed with HFSS for

the CPW and microstrip configurations shown in Fig. 5. A study of the boundary conditions for the 18- μm line width is summarized in Table III, whose last column represents the configuration used in the device under test. To incorporate the effects of the kinetic inductance in the simulation, a surface inductance per square, L_k^\square , was introduced.⁴⁹ Waveports matched to the transmission line impedance and an S -parameter amplitude convergence $\Delta S < 0.01$ were employed in the finite-element simulations. By comparing to analytical expressions for microstrip geometries, a conservative systematic error of $< 2\%$ was estimated for the simulated

TABLE III. HFSS simulations—Superconducting microstrip transmission line (18- μm line width).^a

Transmission line conductor, model definition	Perfect-E	Perfect-E	Nb	Mo_2N	
Line surface inductance, L_k^\square (line)	0.12	4.3	(pH/ \square)
Line metallization thickness	0.25	0.07	(μm)
Ground plane conductor, model definition	Perfect-E	Perfect-E	Nb	Nb	
Ground plane surface inductance, L_k^\square (ground)	0.12	0.13	(pH/ \square)
Ground plane metallization thickness	0.50	0.50	(μm)
Superstrate relative permittivity, ϵ_1/ϵ_0	1.000	1.000	1.000	1.000	(-)
Substrate relative permittivity, ^b ϵ_2/ϵ_0	1.000	11.55	11.55	11.55	(-)
Transmission line impedance, Z_0 , HFSS	8.5(0)	2.6(1)	3.1(1)	7.8(4)	(Ω)
Relative wave impedance, $Z_n = (\mu_{r,\text{eff}}/\epsilon_{r,\text{eff}})^{1/2}$	1.00(0) ^c	0.307	0.366	0.922	(-)
Effective index, $n_{\text{eff}} = (\epsilon_{r,\text{eff}} \cdot \mu_{r,\text{eff}})^{1/2}$	1.00(2)	3.293	3.999	10.67	(-)
Effective relative permittivity, $\epsilon_{r,\text{eff}} = n_{\text{eff}}^2/Z_n$	1.00(2)	10.73	10.93	11.57	(-)
Effective relative permeability, $\mu_{r,\text{eff}} = n_{\text{eff}} \cdot Z_n$	1.00(2)	1.0(1)	1.463	9.844	(-)
Kinetic inductance fraction, $\alpha = 1 - 1/\mu_{r,\text{eff}}$	0.00(2)	0.0(1)	0.317	0.898	(-)

^aThe upper portion of the table contains the simulation input parameters and the lower portion contains the computed and derived results.

^bFor the simulations presented, the input dielectric function for silicon was specified as lossless for simplicity.

^cThe last significant digit computed in HFSS simulations is indicated with parentheses for selected entries. Deviation from zero is suggestive of the magnitude of the systematic error encountered in simulation of the transmission line structures.

parameters derived from HFSS. Similar estimates arise from consideration of the magnitude of the constitutive relations derived from the simulations in the limit where the dielectric materials are replaced by free space and metallization layers are perfect-electric field boundaries.

To study the resonator circuit's response in detail, a fit of the $S_{21, \text{res}}$ data depicted in Fig. 3(e) to Eq. (A2) was performed. The fitting parameters were Z_o , n_{eff} , and C_c for each of the two resonators' transmission line sections. From Z_o , the medium's relative wave impedance, Z_n , can be determined as follows:

$$Z_n \equiv \left(\frac{\mu_{r, \text{eff}}}{\varepsilon_{r, \text{eff}}} \right)^{1/2} = \frac{Z_o}{Z_{o, \text{HFSS}}} \quad (8)$$

for each of the transmission lines used in the resonator realization. Here, $Z_{o, \text{HFSS}}$ represents the transmission line characteristic impedance simulated using HFSS with perfect E-field boundaries for conductors and the permittivity of free space for dielectrics.

From Eq. (6) and Eq. (8), it follows that the effective permittivity and permeability are related by

$$\varepsilon_{r, \text{eff}} = n_{\text{eff}}/Z_n, \quad \mu_{r, \text{eff}} = n_{\text{eff}} \cdot Z_n. \quad (9)$$

These scaling relationships between $\varepsilon_{r, \text{eff}}$ and $\mu_{r, \text{eff}}$ were enforced by the algorithm during fitting. The resulting transmission response computed with this methodology [see Eq. (A2)] agrees with the measured data within 1%, similarly to the accuracy previously found through the evaluation of Eq. (3). This analysis approach is analogous to that implemented in Ref. 50 to explicitly link the transmission line parameters which depend upon the detailed sample geometry to the interaction of the fields in a homogeneous bulk material sample in an electromagnetically self-consistent manner. For example, a non-physical dielectric function would be encountered if $\mu_{r, \text{eff}} \equiv 1$ was tacitly adopted for the superconducting material.^{51,52}

A parameter of interest for superconducting resonator-based detectors is the kinetic inductance fraction,⁵³ α , which is defined as the ratio of the transmission line's kinetic inductance, $L(\mu_1, \mu_2) - L(\mu_o, \mu_o)$, relative to the total inductance, $L(\mu_1, \mu_2)$. With these definitions and through the use of Eq. (7), one obtains

$$\alpha = 1 - \frac{1}{\mu_{r, \text{eff}}}. \quad (10)$$

The results found for α are in quantitative agreement with the values derived from the HFSS simulations (Table III) and can be found in Table IV.

TABLE IV. Transmission line parameter extraction—2-resonator ABCD-matrix model.

Line	$Z_{o, \text{HFSS}}$ (Ω)	Z_o (Ω)	n_{eff} (-)	α (-)
1, low	2.7(0) ^a	2.47 ± 0.01	10.697 ± 0.571	0.898 ± 0.008
1, high	8.5(0)	7.70 ± 0.10	11.143 ± 0.336	0.901 ± 0.007
2, low	2.7(0)	2.47 ± 0.01	10.701 ± 0.162	0.898 ± 0.004
2, high	8.5(0)	7.70 ± 0.03	11.147 ± 0.084	0.901 ± 0.003

^aThe last significant digit computed in HFSS simulations is indicated with parentheses.

VII. CONCLUSIONS

This work presented a methodology to calibrate the transmission response of superconducting microwave resonators at cryogenic temperatures and described two methods to analyze the resulting dataset. The phenomenological and ABCD-matrix methods recovered the measured transmission data with the same 1% level of accuracy, thus providing a numerical validation of the general approach. The derived Q factors in either approach were statistically indistinguishable.

It is interesting to compare the number of parameters required by each method. The first analysis method employs a rational polynomial function of degree k with $2k$ complex and 2 real parameters for each resonator. A second-order function with 6 parameters per resonator was shown to recover the measured data to within a 1% accuracy. The second method, based upon an analysis of the circuit's distributed network, was implemented via cascaded ABCD matrices. Here, 2 complex and 3 real parameters were necessary to compute the ABCD matrices of each transmission line section used to represent the resonator structure and the feedline. In addition, the line lengths were taken as known and the constraint between the wave impedance and the effective index was enforced in fitting. Broadly speaking, the two approaches have comparable underlying complexity.

While the phenomenological model is useful in providing the values of the resonators' central frequencies and widths, the ABCD-matrix method provides insight into the circuit's internal structure when used in conjunction with electromagnetic simulation tools, to make an explicit linkage between the model and the underlying geometric details of the transmission media in use. This approach can be of particular value in extracting the line parameters required for precision circuit design. More importantly, the ABCD-matrix model naturally enables the treatment of distributed transmission line structures without the approximations typically employed in conventional lumped-circuit analysis. The accuracy of these analysis methods exceeds that of a simple lumped-circuit approximation over the frequency span and parameter range experimentally explored.

ACKNOWLEDGMENTS

We acknowledge financial support from the NASA ROSES/APRA program and the Massachusetts Institute of Technology "Arthur Gelb" fellowship. We would like to thank Amil Patel for sample fabrication as well as David Chuss, Negar Ehsan, Omid Noroozian, Jack Sadleir, and Thomas Stevenson for helpful conversations and contributions to this work.

APPENDIX: ABCD-MATRIX MODEL

The ABCD matrix for a two-port network is defined in terms of the total voltages and currents as follows:^{33,54}

$$\begin{bmatrix} V_{in} \\ I_{in} \end{bmatrix} = \begin{bmatrix} A & B \\ C & D \end{bmatrix} \begin{bmatrix} V_{out} \\ I_{out} \end{bmatrix}. \quad (A1)$$

The scattering parameter S_{21} , also known as the transmission amplitude, t , can be directly related to the ABCD parameters

as⁵⁴

$$S_{21} = \frac{2Z_l}{AZ_l + B + CZ_lZ_s + DZ_s}, \quad (\text{A2})$$

where Z_l and Z_s represent the load and source impedances, respectively. The ABCD matrix of the cascade connection of multiple networks is equal to the product of the ABCD matrices representing the individual two-ports, that is,

$$\begin{bmatrix} A & B \\ C & D \end{bmatrix} = \prod_i \begin{bmatrix} A_i & B_i \\ C_i & D_i \end{bmatrix}. \quad (\text{A3})$$

Here, the subscript i is used to indicate the different matrices as well as the ABCD parameters of each matrix.

In particular, the ABCD parameters of a two-port circuit represented by a transmission line are^{33,54}

$$\begin{bmatrix} A & B \\ C & D \end{bmatrix}_{TL} = \begin{bmatrix} \cosh(\gamma l) & Z_o \cdot \sinh(\gamma l) \\ 1/Z_o \cdot \sinh(\gamma l) & \cosh(\gamma l) \end{bmatrix}. \quad (\text{A4})$$

In Eq. (A4), Z_o is the characteristic impedance, γ the propagation constant, and l the line length. The determinant of this matrix is unity.

Each resonator is made of a low-, high-, and low-impedance transmission line connected to a coupling capacitor (Fig. 5). The resonator's low-impedance transmission line section termination was modeled as an open-circuited line, i.e., $Z_{in,1} = Z_l \coth(\gamma l_1)$, while the high- and second low-impedance transmission lines were specified by³³

$$Z_{in,j} = Z_j \frac{Z_{in,j-1} \cosh(\gamma_j l_j) + Z_j \sinh(\gamma_j l_j)}{Z_{in,j-1} \sinh(\gamma_j l_j) + Z_j \cosh(\gamma_j l_j)}, \quad j = 2, 3. \quad (\text{A5})$$

Finally, the total impedance as seen through the coupling capacitors is $Z_{tot} = 1/(i\omega C_c) + Z_{in,3}$. Here, the index j specifies the internal lines in the stepped-impedance resonator. The ABCD matrix associated with the complete resonator structure is therefore

$$\begin{bmatrix} A & B \\ C & D \end{bmatrix}_{res} = \begin{bmatrix} 1 & 0 \\ 1/Z_{tot} & 1 \end{bmatrix}. \quad (\text{A6})$$

The individual resonators are connected to the feedline via a T-junction at their respective electrical delays. The following expression,

$$\begin{bmatrix} A & B \\ C & D \end{bmatrix}_{T-junc} = \begin{bmatrix} A & B \\ C & D \end{bmatrix}_{TL} \begin{bmatrix} A & B \\ C & D \end{bmatrix}_{res} \begin{bmatrix} A & B \\ C & D \end{bmatrix}_{TL}, \quad (\text{A7})$$

allows the resonators to be cascaded with the feedline sections, whose ABCD matrices are expressed through Eq. (A4). The resulting two-port circuit is used to compute the frequency response of the chip. The wire bonds, transition board, connectors, and coaxial cables between the device reference and the instrument termination planes were added in a similar fashion to investigate the baseline response. For simplicity, we do not explicitly treat the parasitic reactance at the transmission line junctions; however, this detail can readily be incorporated in the formulation and can be of importance at higher frequencies. The complex phase velocity and kinetic inductance fraction of the transmission line configuration employed

can be extracted from the response of this composite ABCD-matrix for the system.

- ¹A. Monfardini, A. Benoit, A. Bideaud, N. Boudou, M. Calvo, P. Camus, C. Hoffmann, F.-X. Désert, S. Leclercq, M. Roesch, K. Schuster, P. Ade, S. Doyle, P. Mauskopf, E. Pascale, C. Tucker, A. Bourrion, J. Macias-Perez, C. Vescovi, A. Barishev, J. Baselmans, L. Ferrari, S. J. C. Yates, A. Cruciani, P. De Bernardis, S. Masi, C. Giordano, B. Marghesin, H. Leduc, and L. Swenson, *J. Low Temp. Phys.* **167**, 834 (2012).
- ²J. Schlaerth, N. Czakon, P. Day, T. Downes, R. Duan, J. Glenn, S. Golwala, M. Hollister, H. LeDuc, P. Maloney, B. Mazin, H. Nguyen, O. Noroozian, J. Sayers, S. Siegel, and J. Zmuidzinas, *J. Low Temp. Phys.* **167**, 347 (2012).
- ³L. J. Swenson, P. K. Day, C. D. Dowell, B. H. Eom, M. I. Hollister, R. Jarrot, A. Kovács, H. G. Leduc, C. M. McKenney, R. Monroe, T. Mroczkowski, H. T. Nguyen, and J. Zmuidzinas, *Proc. SPIE* **8452**, 84520P–84520P–10 (2012).
- ⁴B. A. Mazin, B. Bumble, S. R. Meeker, K. O'Brien, S. McHugh, and E. Langman, *Opt. Express* **20**, 1503 (2012).
- ⁵J. Zmuidzinas, *Annu. Rev. Condens. Matter Phys.* **3**, 169 (2012).
- ⁶R. Vijay, D. H. Slichter, and I. Siddiqi, *Phys. Rev. Lett.* **106**, 110502 (2011).
- ⁷J. Krupka, K. Derzakowski, M. Tobar, J. Hartnett, and R. G. Geyer, *Meas. Sci. Technology* **10**, 387 (1999).
- ⁸D. E. Oates, A. C. Anderson, and P. M. Mankiewich, *J. Supercond.* **3**, 251 (1990).
- ⁹P. J. Petersan and S. M. Anlage, *J. Appl. Phys.* **84**, 3392 (1998).
- ¹⁰I. J. Bahl, *Lumped Elements for RF and Microwave Circuits* (Artech House, 2003).
- ¹¹J. Gao, "The Physics of Superconducting Microwave Resonators," Ph.D. thesis, California Institute of Technology, 2008.
- ¹²M. S. Khalil, M. J. A. Stoutimore, F. C. Wellstood, and K. D. Osborn, *J. Appl. Phys.* **111**, 054510 (2012).
- ¹³K. Geerlings, S. Shankar, E. Edwards, L. Frunzio, and M. H. Devoret, *Appl. Phys. Lett.* **100**, 192601 (2012).
- ¹⁴A. Megrant, C. Nelli, R. Barends, B. Chiaro, Y. Chen, L. Feigt, J. Kelly, E. Lucero, M. Mariantoni, P. J. J. O'Malley, D. Sank, A. Vainsencher, J. Wenner, T. C. White, Y. Yin, C. J. Zhao, J. Palmstrom, J. M. Martinis, and A. N. Cleland, *Appl. Phys. Lett.* **100**, 113510 (2012).
- ¹⁵C. Deng, M. Otto, and A. Lupascu, *J. Appl. Phys.* **114**, 054504 (2013).
- ¹⁶L. J. Swenson, P. K. Day, B. H. Eom, H. G. Leduc, N. Llombart, C. M. McKenney, O. Noroozian, and J. Zmuidzinas, *J. Appl. Phys.* **113**, 104501 (2013).
- ¹⁷Z. Ma, Ph.D. thesis (Ginzton Labs Report No. 5298), Stanford University, 1995.
- ¹⁸H. J. Snortland, Ph.D. thesis (Ginzton Labs Report No. 5552), Stanford University, 1997.
- ¹⁹D. Russell, K. Cleary, and R. Reeves, *Rev. Sci. Instrum.* **83**, 044703 (2012).
- ²⁰L. Ranzani, L. Spietz, Z. Popovic, and J. Aumentado, *Rev. Sci. Instrum.* **84**, 034704 (2013).
- ²¹J.-H. Yeh and S. M. Anlage, *Rev. Sci. Instrum.* **84**, 034706 (2013).
- ²²A. Patel, A.-D. Brown, W.-T. Hsieh, T. R. Stevenson, S. H. Moseley, K. U-Yen, N. Ehsan, E. M. Barrentine, G. Manos, and E. J. Wollack, *IEEE Trans. Appl. Supercond.* **23**, 1051 (2013).
- ²³E. J. Wollack, D. T. Chuss, K. Rostem, and K. U-Yen, *Rev. Sci. Instrum.* **85**, 034702 (2014).
- ²⁴P. I. Somlo and J. D. Hunter, *Microwave Impedance Measurement* (Peter Pergrinus Ltd., 1985), pp. 25–31.
- ²⁵R. J. Allen, *Astron. Astrophys.* **3**, 316 (1969), available online at <http://adsabs.harvard.edu/abs/1969A%26A.....3..316A>.
- ²⁶P. F. Goldsmith and N. Z. Scoville, *Astron. Astrophys.* **82**, 337 (1980), available online at <http://adsabs.harvard.edu/abs/1980A%26A.....82..337G>.
- ²⁷P. G. Roll and D. T. Wilkinson, *Ann. Phys.* **44**, 289 (1967).
- ²⁸U. Fano, *Il Nuovo Cimento* **12**, 154 (1935).
- ²⁹U. Fano, *Phys. Rev.* **124**, 1866 (1961).
- ³⁰M. V. Marquezini, P. Kner, S. Bar-Ad, J. Tignon, and D. S. Chemla, *Phys. Rev. B* **57**, 3745 (1998).
- ³¹R. Singh, I. Al-Naib, W. Cao, C. Rockstuhl, M. Koch, and W. Zhang, *IEEE Trans. Terahertz Sci. Technol.* **3**, 820 (2013).
- ³²V. Giannini, Y. Francescano, H. Amrania, C. C. Phillips, and S. A. Maier, *Nano Lett.* **11**, 2835 (2011).
- ³³D. M. Pozar, *Microwave Engineering*, 4th ed. (John Wiley and Sons, Inc., 2011).
- ³⁴A. H. Zemanian, *IEEE Trans. Circuit Theory* **10**, 265 (1963).
- ³⁵J. S. Toll, *Phys. Rev.* **104**, 1760 (1956).
- ³⁶J. D. Jackson, *Classical Electrodynamics* (Wiley, 1975), Chap. 8.8.

- ³⁷S. Probst, F. B. Song, P. A. Bushev, A. V. Ustinov, and M. Weides; e-print [arXiv:1410.3365](https://arxiv.org/abs/1410.3365) [cond-mat.supr-con] (2014).
- ³⁸T. F. Coleman and Y. Li, *SIAM J. Optim.* **6**, 418 (1996).
- ³⁹T. F. Coleman and Y. Li, *Math. Program.* **67**, 189 (1994).
- ⁴⁰D. Kajfez and E. Hwan, *IEEE Trans. Microwave Theory Tech.* **32**, 666 (1984).
- ⁴¹A. Canos, J. Catala-Civera, F. Penaranda-Foix, and E. Reyes-Davo, *IEEE Trans. Microwave Theory Tech.* **54**, 3407 (2006).
- ⁴²R. F. Bauer, Jr. and P. Penfield, *IEEE Trans. Microwave Theory Tech.* **22**, 282 (1974).
- ⁴³A. Vayonakis, C. Luo, H. G. Leduc, R. Schoelkopf, and J. Zmuidzinas, *AIP Conf. Proc.* **605**, 539 (2002).
- ⁴⁴T. M. Weller, L. P. Katehi, and G. M. Rebeiz, *IEEE Microwave Guided Wave Lett.* **5**, 153 (1995).
- ⁴⁵R. F. Harrington, *Field Computation by Moment Methods* (IEEE Press, 1993), Chap. 5.
- ⁴⁶R. K. Hoffmann, *Handbook of Microwave Integrated Circuits* (Artech House, 1987), Chap. 2.
- ⁴⁷Soitec, *Smart cut silicon-On-insulator (SOI) wafer*, 2014.
- ⁴⁸R. Datta, C. Munson, M. Niemack, J. McMahon, J. Britton, E. Wollack, J. Beall, M. Devlin, J. Fowler, P. Gallardo, J. Hubmayr, K. Irwin, L. Newburgh, J. Nibarger, L. Page, M. Quijada, B. Schmitt, S. Staggs, R. Thornton, and L. Zhang, *Appl. Opt.* **52**, 8747 (2013).
- ⁴⁹A. R. Kerr, "Surface impedance of superconductors and normal conductors in EM simulators," Millimeter Array (MMA) Technical Report No. 245 (National Radio Astronomy Observatory, 1999).
- ⁵⁰D. T. Chuss, E. J. Wollack, R. Henry, H. Hui, A. J. Juarez, M. Krejny, S. H. Moseley, and G. Novak, *Appl. Opt.* **51**, 197 (2012).
- ⁵¹K. K. Mei and G.-C. Liang, *IEEE Trans. Microwave Theory Tech.* **39**, 1545 (1991).
- ⁵²Z.-Y. Shen, *High Temperature Superconducting Microwave Circuits* (Artech House, Boston, Massachusetts, 1994), Section 3.3.3.
- ⁵³A. Porch, P. Mauskopf, S. Doyle, and C. Dunscombe, *IEEE Trans. Appl. Supercond.* **15**, 552 (2005).
- ⁵⁴P. F. Goldsmith, *Quasioptical Systems: Gaussian Beam Quasioptical Propagation and Applications* (IEEE Press, 1998), pp. 231–235.